IEEE Access
Multidisciplinary ⋮ Rapid Review ⋮ Open Access Journal

Received May 19, 2022, accepted June 5, 2022, date of publication June 15, 2022, date of current version June 22, 2022.

Digital Object Identifier 10.1109/ACCESS.2022.3183347

Fault Mechanism Analysis of Irreversible Demagnetization Due to the Dynamic Eccentricity of IPMSM for EV Traction

JUN-KYU KANG, (Student Member, IEEE), AND JIN HUR, (Fellow, IEEE)
Department of Electrical Engineering, Incheon National University, Incheon 22012, Republic of Korea

Corresponding author: Jin Hur (jinhur@inu.ac.kr)

This work was supported in part by the Industrial Strategic Technology Development Program of Korea Evaluation Institute of Industrial Technology (KEIT) under Grant 20010132 and Grant 20018501.

ABSTRACT The dynamic eccentricity fault (DEF) of the interior permanent magnet synchronous motor (IPMSM) is mainly caused by external mechanical shock. In the case of DEF, an unbalanced magnetic force occurs because the length of the air gap is not constant. Noise and vibration of the motor occur due to unbalanced magnetic force. In addition, since the length of the air gap is not constant, the distribution of magnetic flux density is distorted, and iron loss is increased. As the iron loss increases, the temperature rises, and an irreversible demagnetization fault (IDF) of the permanent magnet occurs due to overheating. Therefore, in this paper, the fault mechanism of IDF due to DEF of IPMSM for electric vehicle (EV) traction is analyzed. Initially, the magnetic flux density and iron loss characteristics according to the healthy condition and DEF condition are analyzed using the finite element method (FEM). Then, the detailed iron loss analysis is performed based on the phase current waveform measured through the load test of the motor. Finally, the fault mechanism of IDF due to DEF was verified through an electric-axle load test on a manufactured motor having eccentricity.

INDEX TERMS Dynamic eccentricity, electric vehicle (EV), interior permanent magnet synchronous motor (IPMSM), iron loss, irreversible demagnetization.

I. INTRODUCTION

Recently, for the development of optimized electric vehicles (EVs) according to environmental regulation problems, research on the driving system and the energy storage system, in order to replace the engine of the existing vehicle, is being actively conducted. In particular, it is one of the important issues to optimize driving safety and increase the driving range of EVs by using an optimized traction motor in the EV drive system. To satisfy the requirements of these traction motors, the number of vehicles using interior permanent magnet synchronous motors (IPMSMs) is increasing [1]–[5]. IPMSM has the characteristics of high efficiency and high torque density and has the advantage of being able to operate in a relatively wide high-speed range through field-weakening control. In addition, it has the advantage of high mechanical safety during high-speed operation by inserting a permanent magnet into the iron core of the rotor [6]–[8].

The associate editor coordinating the review of this manuscript and approving it for publication was Shihong Ding.

However, a fault may occur due to a mechanical shock transmitted to the electric motor from the outside, and the reliability and lifespan of the electric motor may reduce due to an electrical defect. Common types of faults in IPMSM include irreversible demagnetization fault (IDF) of permanent magnets, stator inter-turn fault (SITF) in the stator winding, and mechanical faults such as eccentricity fault (EF) and bearing fault in which the centers of rotation of the stator and rotor are not aligned [9]–[27]. IDF occurs due to an increase in the rotor temperature and a reverse magnetic field because of the excessive current flowing during the load operation of the motor [9]–[11]. SITF is a short circuit fault between adjacent windings of a stator, due to the thermal, mechanical, and electrical damage in the stator windings which affects the insulation of the windings [12]–[14]. EF occurs when the rotational axis of the rotor and the axis center of the stator do not match. EF is of two types; a static eccentricity fault (SEF) and a dynamic eccentricity fault (DEF). In the case of SEF, the rotation axis of the rotating rotor and the axis center of the stator do not match, but the rotation center

of the rotor is constant, and the non-uniform magnetic flux density distribution appears depending on the severity of the eccentricity. In contrast, in the case of DEF, the rotor rotates around the same axis as the stator axis, but the rotation axis does not match the axis of the rotor [15]–[18]. That is, when the rotor rotates in the DEF situation, the length of the air gap is changed, and an unbalanced magnetic force is generated according to rotation. As a result, serious damage to the motor is caused and a bearing defect may occur. In addition, if the motor rotates for a long time in the DEF state, an unbalanced electromagnetic force is generated, which produces noise and vibration. In such a serious condition, the cage of the ball bearing is damaged and the insulation of the stator winding is also damaged [19]–[26]. From another point of view, in the DEF condition, since the length of the air gap changes with rotation, the air gap flux density becomes unbalanced. This unbalanced magnetic flux density affects the iron loss of the motor. In general, IPMSM operates at a magnetic saturation point, so there are many harmonic components, but under the DEF condition, the harmonic components increase further due to distortion of the magnetic flux density. As a result, iron loss increases more in the DEF state than in the healthy condition. As the speed of the motor increases, the iron loss also increases, affecting the efficiency and reliability of the motor. Moreover, as the iron loss from the iron core increases, the temperature rises, and if the motor is driven in the DEF state for a long time, irreversible demagnetization of the permanent magnet in the rotor may occur due to overheating inside the motor [27]–[31].

In this study, the characteristics of iron loss according to the DEF condition of IPMSM for traction of EVs and the characteristics of irreversible demagnetization of the permanent magnet are analyzed.

In particular, when IDF occurs, more current is applied under the same load conditions. Because of this phenomenon, the efficiency of the motor decreases due to increased losses. In addition, the temperature of the motor and the inverter also increases, which can degrade the reliability of the system and cause serious failures. Therefore, this paper presents a fault mechanism that shows that DEF can cause IDF as well as affect the noise and vibration of electric motors.

The contributions of this paper can be summarized here.

- In the DEF condition, the air gap flux density is unbalanced due to a continuous change in air gap length according to the rotation. Because of this phenomenon, the iron loss increases further due to the distortion of the magnetic flux density. The iron loss analysis was performed in the healthy and the DEF condition based on the measured raw current waveforms, using the Ansys Maxwell software. The analysis results show that the iron loss increases under the DEF condition. In particular, it shows that the iron loss increases in the high-speed region than in the low-speed region.
- The fault mechanism of IDF by DEF was verified through the load test of the electric axle to which the manufactured DEF motor was applied.

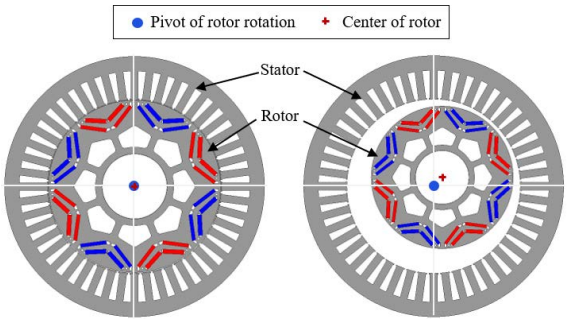

FIGURE 1. Definition of the model, (a) base model, (b) DEF model.

TABLE 1. Motor specifications.

Items	Unit	Value
Number of poles	-	8
Number of slots	-	48
Stator outer radius	mm	250
core material	-	30PNF1600
Maximum rated torque	Nm	300
Rated speed	RPM	2,550
Maximum speed	RPM	10,000
Air gap	mm	0.8
Maximum rated power	kW	80

The paper is comprised of the following sections: Initially, The magnetic flux density and the iron loss analysis according to the increase in the DEF level using the finite element method (FEM) will be described in section II. Here, when the speed increases in the DEF condition, a change in iron loss is analyzed. Section III describes the analysis of iron loss according to the input current. Section IV describes the loss, efficiency, and temperature analysis according to the healthy and DEF conditions. Section V describes the verification of IDF phenomenon due to DEF.

II. IPMSM MODEL CONSIDERING DEF

A. COMPARISON OF MAGNETIC FLUX DENSITY BETWEEN BASE MODEL AND DEF MODEL

The base model of IPMSM for EV traction was designed as shown in Figure 1(a). The specifications of the motor are shown in Table 1. The maximum output is 80kW, and the maximum speed is 10,000 RPM. As shown in Figure 1(a), in the case of the base model, the pivot of rotor rotation and the center of rotor coincide. However, in the case of the DEF model, as shown in Figure 1(b), the pivot of rotor rotation and the center of the rotor do not match due to mechanical defects. Therefore, the length of the air gap changes as the rotor rotates. The air gap $\delta(\theta, t)$ can be expressed by [16]

$$\boldsymbol{\delta(\theta, t) = \delta_m\{1 - \varepsilon\cos(\theta - \omega t - \beta)\}} \quad (1)$$

where δ_m is the average air gap length, ε is the eccentricity, ω is the rotational angular velocity of the rotor, and β is the initial phase angle of the eccentricity.

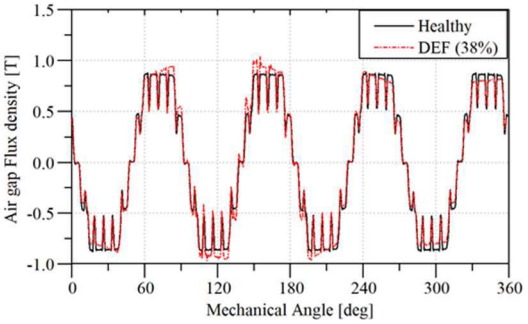

FIGURE 2. Air gap flux density.

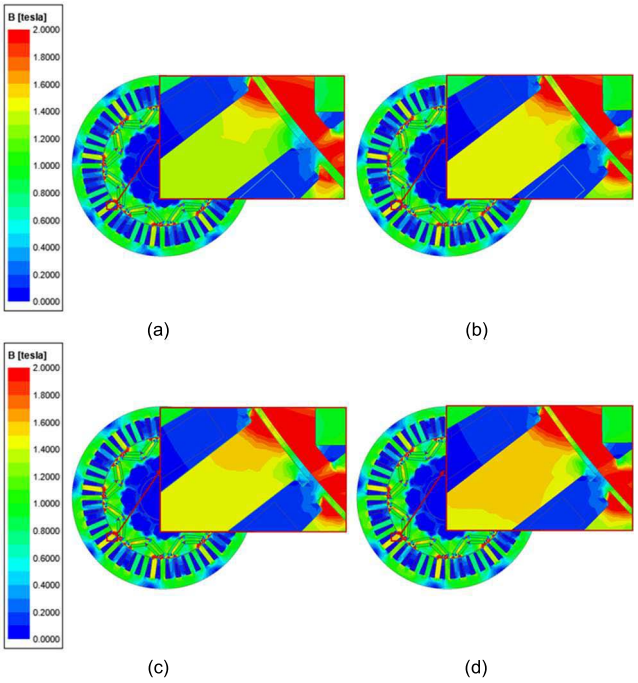

FIGURE 3. Magnetic flux density distribution according to DEF level, (a) Healthy, (b) DEF (20%), (c) DEF (30%), (d) DEF (38%).

The permeance of the air $\Lambda(\theta, t)$ can be expressed by

$$\Lambda(\theta, t) = \frac{1}{\delta(\theta, t)} = \frac{1}{\delta_m\{1 - \varepsilon\cos(\theta - \omega t - \beta)\}} \quad (2)$$

Magnetic flux density $B(\theta, t)$ can be expressed by

$$B(\theta, t) = \mu_0 F_{mmf}(\theta, t)\,\Lambda(\theta, t) \quad (3)$$

where μ_0 is the permeability of air, and F_{mmf} is the magnetomotive force. Therefore, due to DEF, the length of the air gap is not constant, so the magnetic flux density changes. Figure 2 shows the waveform of the air gap flux density. In the case of the healthy condition, the air gap flux density waveform is balanced. However, in the case of the DEF condition, the air gap flux density waveform is unbalanced. The eccentricity level of the analysis model of the DEF condition was set to 38%. As shown in Figure 2, the air gap flux density in the DEF condition contains higher harmonics than the air gap flux density in the healthy condition, so the motor characteristics are also changed due to DEF.

Figure 3 shows the magnetic flux density distribution according to the DEF level. Figure 3(a) is a healthy condition, and as shown in Figure 3(b), Figure 3(c), and Figure 3(d), the length of the air gap changes as the DEF level increases. Accordingly, the degree of saturation of the magnetic flux density distribution also increases.

B. FEM ANALYSIS ACCORDING TO OPERATING POINT

Figure 4 shows the torque and speed curve of the motor. As shown in Figure 4, the curve of 80kW has the maximum output and the curve of 50kW shows the rated output.

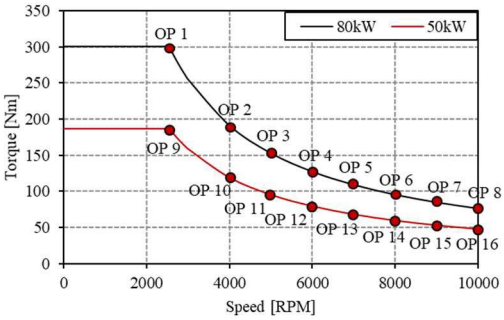

FIGURE 4. Torque and speed curve of the traction motor.

TABLE 2. Definition by operating point.

Operating point	Power [kW]	Speed [RPM]	Current [A_{rms}]	Current angle [°]
OP 1	80	2,550	448.8	45.8
OP 2	80	4,000	290.1	46
OP 3	80	5,000	253.3	52.5
OP 4	80	6,000	255.1	67.8
OP 5	80	7,000	265	70.4
OP 6	80	8,000	282	74.3
OP 7	80	9,000	288.8	77.6
OP 8	80	10,000	299.9	79.7
OP 9	50	2,550	283.5	40
OP 10	50	4,000	189.9	40
OP 11	50	5,000	159.1	42.6
OP 12	50	6,000	166.6	60
OP 13	50	7,000	187.3	70.3
OP 14	50	8,000	209.3	76
OP 15	50	9,000	229.7	79.4
OP 16	50	10,000	247.8	81.7

In this paper, the iron loss was analyzed by using the FEM analysis based on the iron loss data calculated by the modified Steinmetz equation. As shown in Table 2, FEM analysis was performed to calculate the iron loss according to the DEF level at a total of 16 points. DEF levels are 10%, 20%, 30%

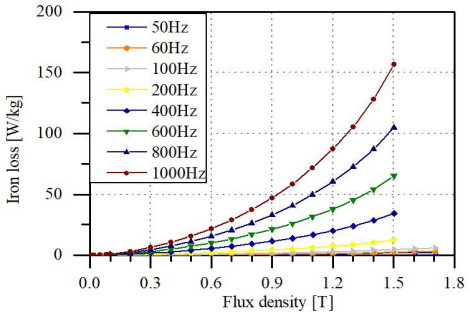

FIGURE 5. Iron loss curves of 30PNF1600.

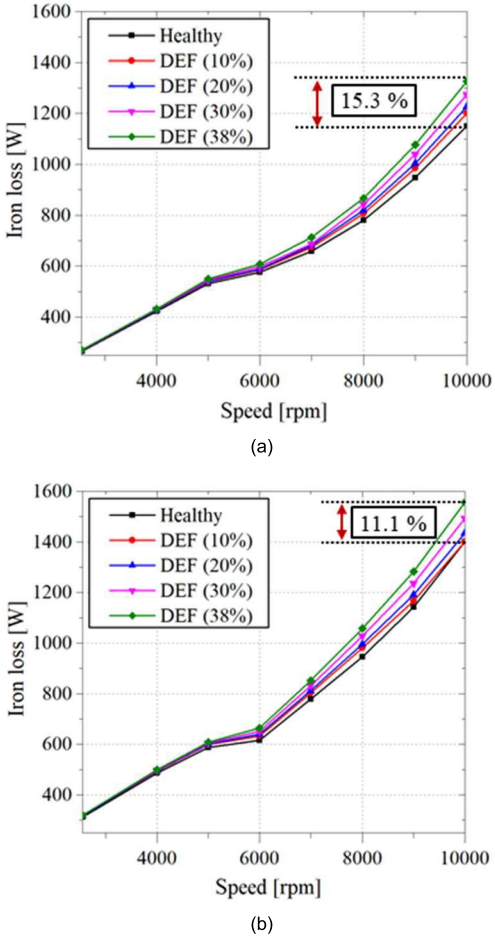

FIGURE 6. Iron loss according to speed, (a) 50kW, (b) 80kW.

and 38%. Figure 5 shows the iron loss curves of 30PNF1600. The Steinmetz equation for calculating the iron loss is shown as follows [32]–[33]

$$W_{iron-loss} = W_h \mathcal{C} W_e \mathcal{C} W_a = k_h f B^2 + k_e f^2 B^2 + k_a f^{1.5} B^{1.5} \quad (4)$$

Iron loss is divided into hysteresis loss (W_h), eddy current loss (W_e), and amorphous loss (W_a). Where k_h is the hysteresis loss coefficient, k_e is the eddy current loss coefficient, and k_a is the anomalous loss coefficient. f is the operating frequency and B is the magnetic flux density.

As shown in Figure 6, the iron loss increases as the DEF level and speed increase. This is because the higher the DEF level, the higher the harmonic component due to the distortion of the magnetic flux density. As shown in Figure 6(a), the iron loss in the DEF (38%) condition increased by 15.3% compared to the iron loss in the healthy condition when the motor output was 50 kW and the speed was 10,000 RPM. Whereas, as shown in Figure 6(b), the iron loss in the DEF (38%) condition increased by 11.1% compared to the iron loss in the healthy condition when the motor output was 80 kW and the speed was 10,000 RPM.

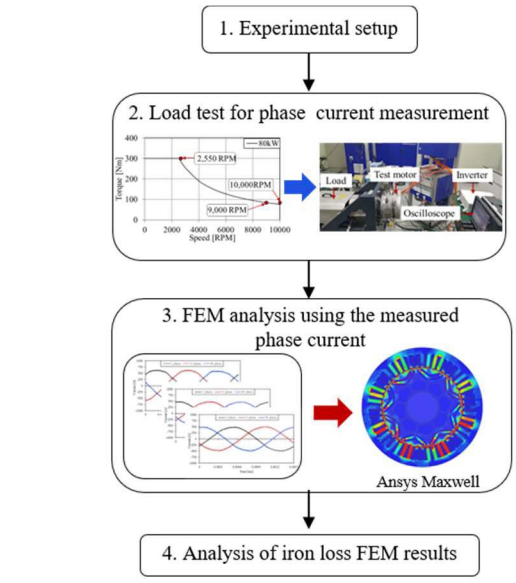

FIGURE 7. Flow chart for raw waveform-based iron loss analysis.

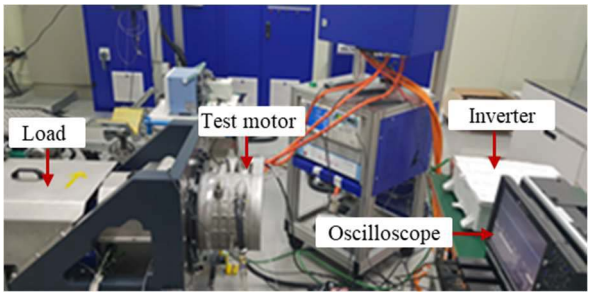

FIGURE 8. Experimental setup.

III. RAW CURRENT WAVEFORM BASED IRON LOSS ANALYSIS

A load test was conducted to analyze the iron loss in the IPMSM in detail. The flow chart for iron loss analysis based on the raw current waveform is shown in Figure 7. First, an experimental setup was performed for the load test as shown in Figure 8. Torque control was performed through an inverter for the load test of the motor. The load test was

FIGURE 9. Teledyne LeCroy current probes (CP500).

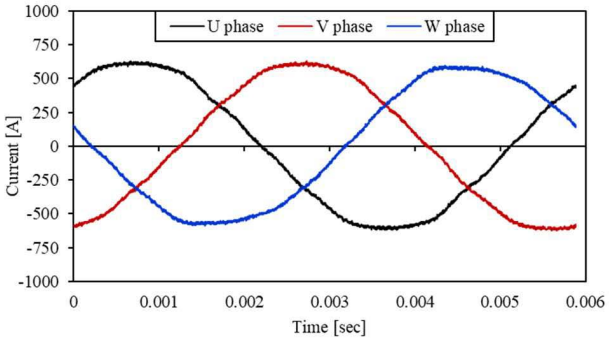

(a)

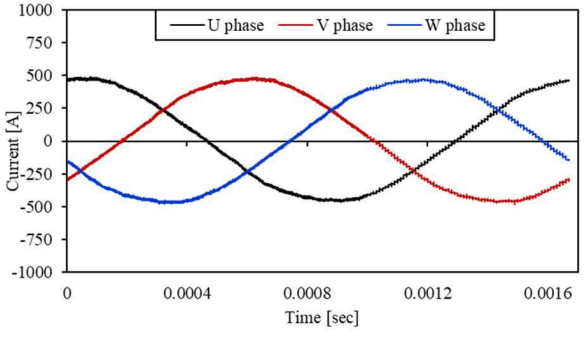

(b)

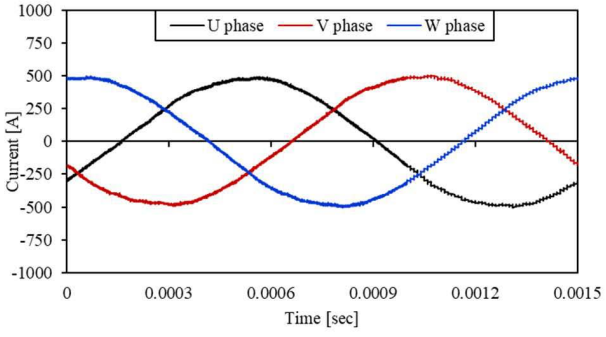

(c)

FIGURE 10. Measured phase current waveform at 80 kW, (a) 2,550 RPM, (b) 9,000 RPM, (c) 10,000 RPM.

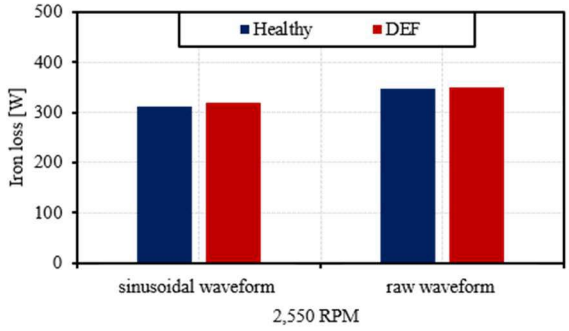

(a)

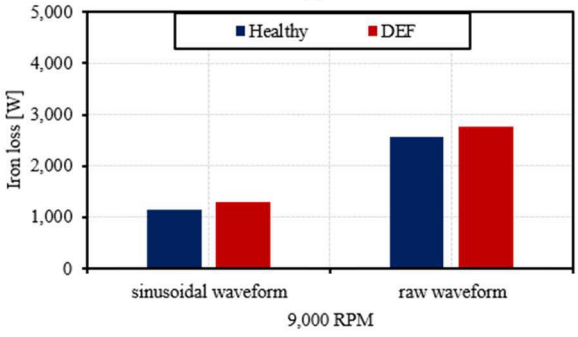

(b)

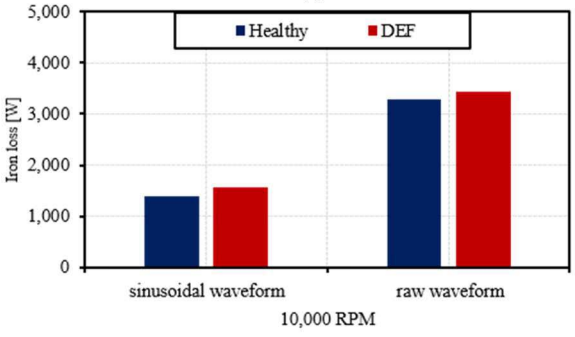

(c)

FIGURE 11. Comparison of iron loss according to input current, (a) 2,550 RPM, (b) 9,000 RPM, (c) 10,000 RPM.

performed at three speeds; 2,550 RPM, 9,000 RPM, and 10,000 RPM at 80 kW maximum output. Additionally, as shown in Figure 9, the current applied to each phase of the motor was measured using Teledyne LeCroy Current Probes (CP500). Based on the current measured through the load test, FEM analysis was performed using Ansys Maxwell software. Finally, the results of iron loss analysis, according to the sinusoidal waveform (SW) and raw waveform (RW) input conditions, were comparatively analyzed. Figure 10 shows the current waveform of each phase measured using the current probe. The switching frequency of the inverter controlling the motor is 8 kHz, and the current waveform including the harmonics of the switching frequency is shown. Figure 10(a) shows the current measured at 2,550 RPM (at 80 kW), Figure 10(b) shows the current measured at 9,000 RPM (at 80 kW), and Figure 10(c) shows the current measured at 10,000 RPM (at 80 kW). Figure 11 shows the comparison of iron loss according to the

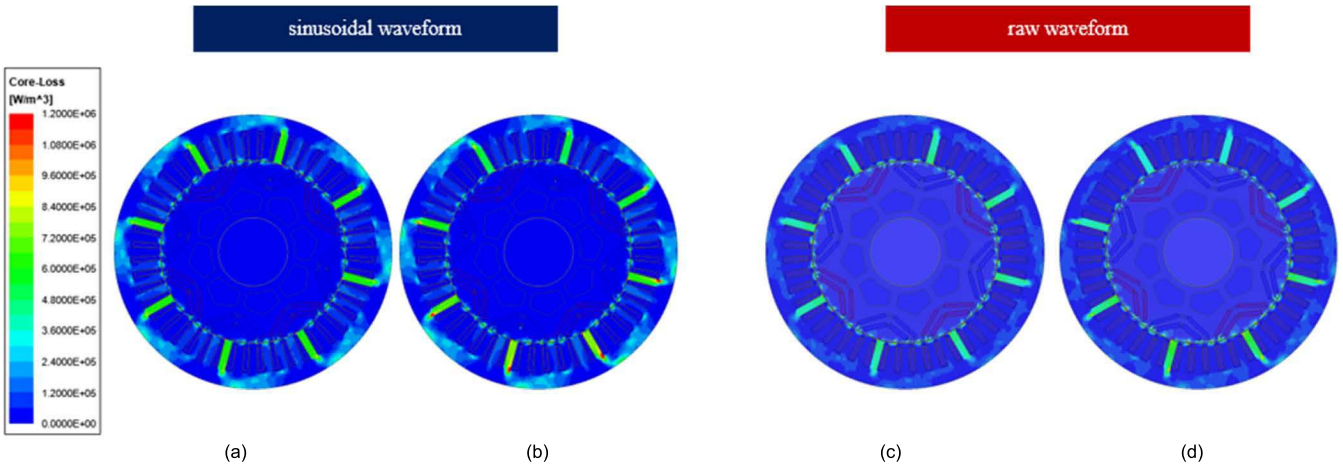

FIGURE 12. Comparison of iron loss at 2,550 RPM, (a) healthy (SW), (b) DEF (38%) (SW), (c) healthy (RW), (d) DEF (38%) (RW).

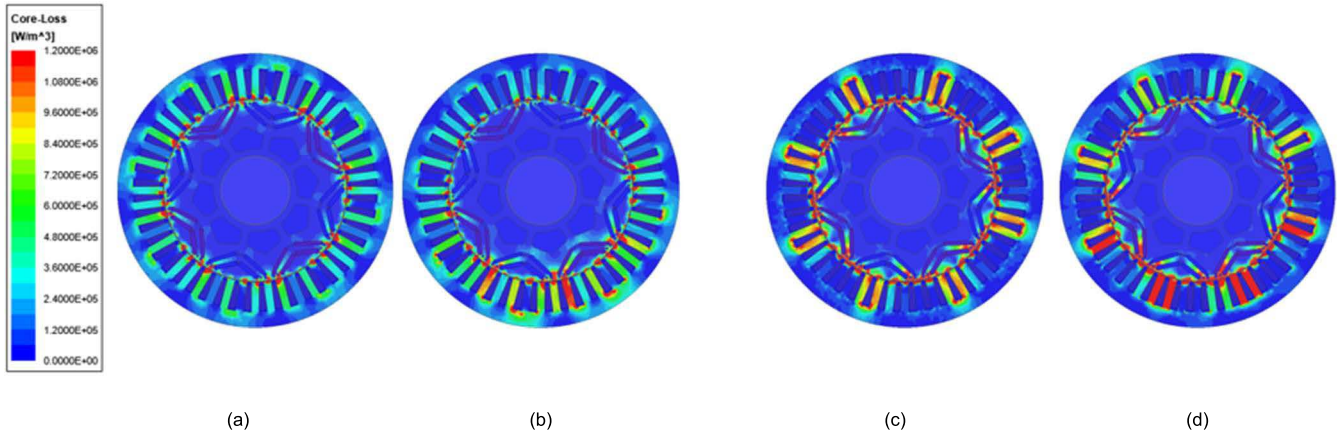

FIGURE 13. Comparison of iron loss at 9,000 RPM, (a) healthy (SW), (b) DEF (38%) (SW), (c) healthy (RW), (d) DEF (38%) (RW).

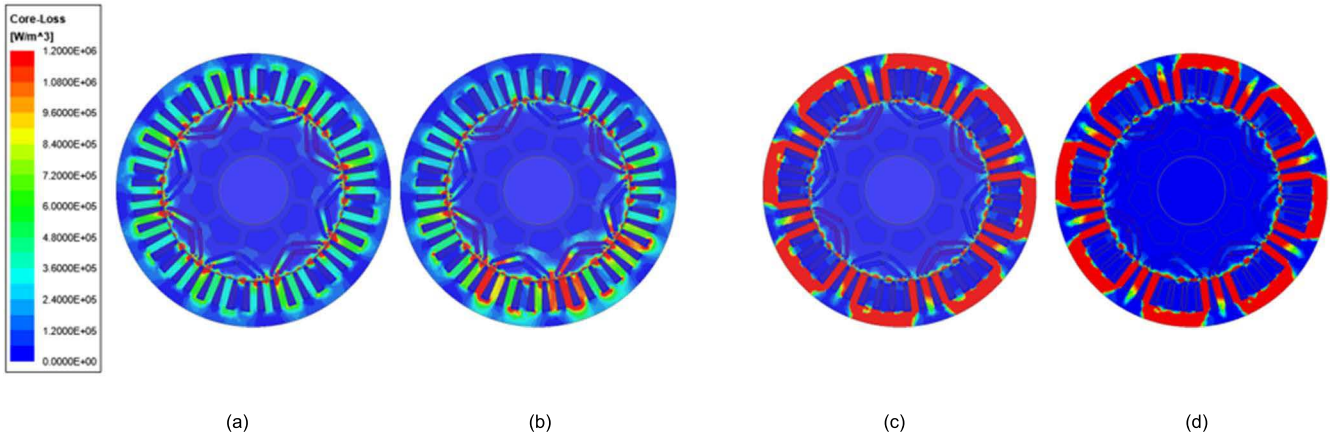

FIGURE 14. Comparison of iron loss at 10,000 RPM, (a) healthy (SW), (b) DEF (38%) (SW), (c) healthy (RW), (d) DEF (38%) (RW).

input current. As shown in Figure 11(a), iron loss in the DEF (38%) condition increased by 2.6% compared to the healthy condition when inputting the ideal SW, and iron loss in the DEF (38%) condition increased by 0.6% compared to the healthy condition when inputting RW. Therefore, in the low-speed region, iron loss increases in the DEF condition, but the increase rate is small. As shown in Figure 11(b), iron loss in the DEF (38%) condition increased by 12.2% compared to the

healthy condition when inputting the ideal SW, and iron loss in the DEF (38%) condition increased by 7.8% compared to the healthy condition when inputting RW. Finally, as shown in Figure 11(c), iron loss in the DEF (38%) condition increased by 11.1% compared to the healthy condition when inputting the ideal SW, and iron loss in the DEF (38%) condition increased by 4.5% compared to the healthy condition when inputting RW. In conclusion, the increased rate of iron loss in the DEF (38%) condition is larger in the high-speed region than in the low-speed region. In addition, since harmonics due to the switching frequency of the inverter are included when the RW is input, iron loss increases as compared to when the SW is input. As shown in Figure 11(a), the iron loss at SW input in the DEF condition was 319.8 W, and the iron loss at RW input was 349.8 W, so it increased by 9.4 %. As shown in Figure 11(b), the iron loss at SW input in the DEF condition was 1,283.1 W, and the iron loss at RW input was 2,760.1 W, so it increased by 115.1 %. As shown in Figure 11(c), the iron loss at SW input in the DEF condition was 1,556.3 W, and the iron loss at RW input was 3,430.4 W, so it increased by 120.4 %. The iron loss according to ideal SW and RW inputs was analyzed through FEM. As shown in Figure 12, there is a little change in the iron loss in the low-speed area of 2,550 RPM. However, as shown in Figure 13 and Figure 14, in the case of inputting SW and RW in the high-speed area, the iron loss increased more in the DEF condition than in the healthy condition. Although the difference in loss seems small in the iron loss distribution as shown in Figure 14, the iron loss in the healthy condition is 3,280 W as shown in Figure 14(c), and the iron loss in the DEF condition is 3,430.4 W as shown in Figure 14(d). Therefore, the harmonic component is increased in the case of the DEF condition, so the iron loss is increased by 4.5 %.

IV. LOSS, EFFICIENCY, AND TEMPERATURE ANALYSIS

This section presents the results of iron loss, efficiency, and thermal analysis. Initially, Figure 15 shows the iron loss map. As shown in Figure 15 (b), in the case of the DEF condition, the difference in the iron loss in the low-speed region is small, but in the high-speed region, as illustrated in a rectangular area, the iron loss increases. As a result, in the case of the DEF condition, as shown in Figure 16(b), the efficiency in the high-speed area as shown in the rectangular is reduced.

Figure 17 shows the results of the thermal analysis based on the loss derived through FEM analysis. Ansys Motor-CAD software based on the thermal equivalent circuit was used [34]. The thermal analysis condition is 80 kW and 10,000 rpm of the motor. The iron loss was selected as the biggest point to see the temperature change of the motor due to the DEF condition. In addition, the copper loss in the healthy condition and DEF (38%) condition is the same. The results of the analysis are shown in Figure 17 and Table 3. The maximum temperature of the winding was 9.2% higher in DEF (38%) than in healthy condition. The maximum temperature of the magnet was 5.9% higher in DEF (38%) as compared to healthy condition. The maximum temperature

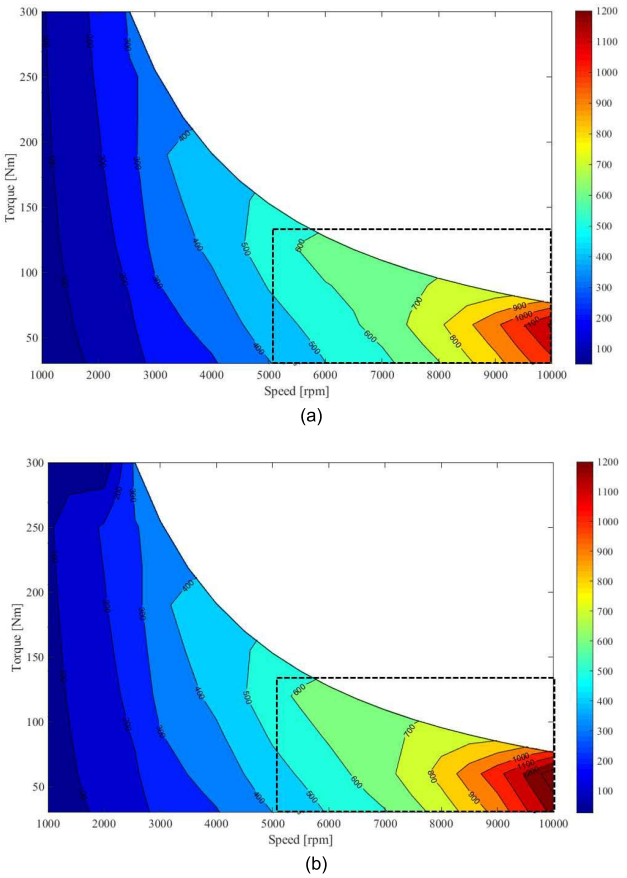

FIGURE 15. Iron loss map, (a) healthy, (b) DEF (38%).

of the stator surface was 9.4% higher in DEF (38%) than in healthy condition. The maximum temperature of the rotor surface was 5.3% higher in DEF (38%) condition than in healthy condition. In conclusion, the overall temperature of important parts of the motor increases due to increased iron loss. And in long-time operation, the irreversible demagnetization of permanent magnets also occurs.

V. VERIFICATION OF IDF PHENOMENON DUE TO DEF

A. ELECTRIC-AXLE LOAD TEST SETUP

In this part, it is presented through a test that the IDF phenomenon occurs due to an excessive increase in heat of the rotor because DEF increases the iron loss of IPMSM. Figure 18 shows the experimental setup to verify the IDF due to DEF in the IPMSM. The test setup is composed of an electric-axle structure in which the DEF motor and the speed reducer are assembled as shown in Figure 18. Figure 19(a) shows the base motor. As shown in Figure 19(b), the bearing pocket part of the rear cover was modified to implement the DEF condition. Where B_h is the diameter of the basic bearing pocket, and B_{DE} is the additional clearance to implement the DEF. B_h is 60mm, and B_{DE} is 0.608mm. The experiment was performed at 8,700 RPM speed and the output of the motor is 50kW. The temperature of the cooling water flowing through

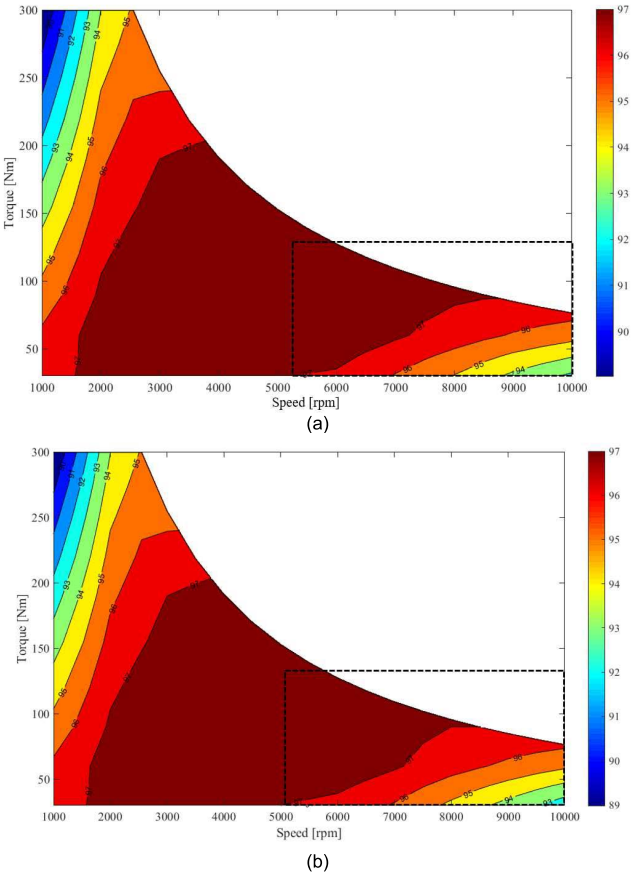

FIGURE 16. Efficiency map, (a) healthy, (b) DEF (38%).

TABLE 3. Thermal analysis results of motor.

Temperature parameters	Healthy	DEF (38%)
Winding	159.2 °C	173.8 °C
Magnet	112.5 °C	119.1 °C
Stator Surface	156.4 °C	171.1 °C
Rotor Surface	102 °C	107.4 °C

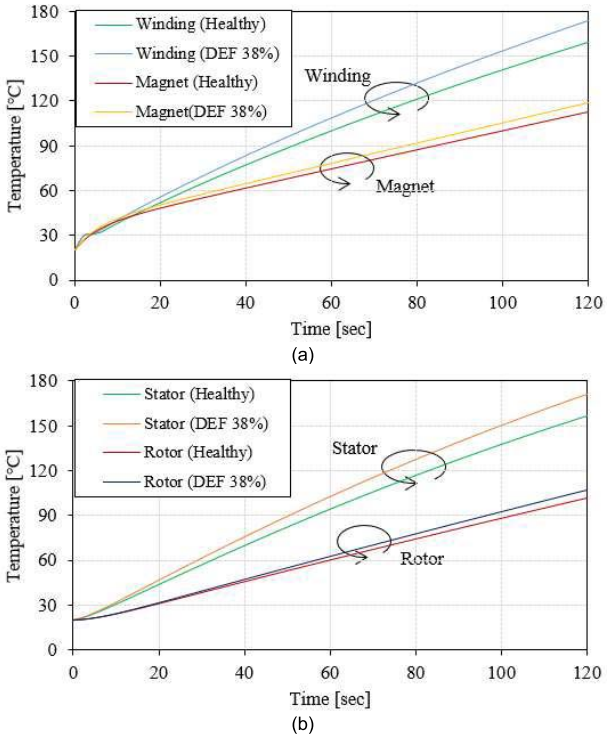

FIGURE 17. Thermal analysis results using MotorCAD, (a) Temperature of winding and permanent magnets, (b) Temperature of stator and rotor.

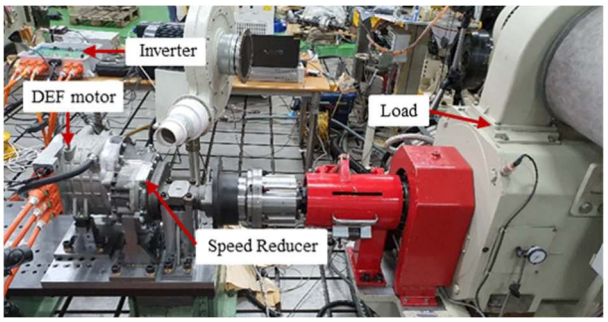

FIGURE 18. Experimental setup with DEF motor.

the motor and inverter is set at 20 °C. The driving time was 114 minutes. Finally, the reduction ratio of the speed reducer is 9.6. Saturation occurred at 6,000 sec at the temperature of the end winding.

B. LOAD TEST RESULTS

Figure 20 shows the torque variations over time. The average torque is 475.1 Nm, and it can be confirmed that the motor is continuously driven. Figure 21 shows the speed of the motor and the temperature of the stator end windings. At this time, the maximum temperature is 153 °C. Accordingly, since the maximum temperature limit of the winding is 170 °C, the experimental value does not exceed the limit.

Figure 22 shows the V_q, V_d voltages of the DEF motor. As shown in Figure 22(a), V_q was initially applied at 104 V but decreased to 74 V at the end of the test. However, as shown in Figure 22(b), the V_d voltage was initially applied at −138.3 V, but at the end of the test, it increased in a negative direction to −153 V. This is because the iron loss increases due to the influence of dynamic eccentricity, resulting in irreversible demagnetization. In particular, when irreversible dema-gnetization occurs, the flux linkage of the permanent magnet decreases, so the d-axis flux linkage decreases, and the q-axis flux linkage increases. Therefore, V_d increases in the negative direction and V_q decreases [9].

Figure 23 shows the back electromotive force (BEMF) waveform of the motor. BEMF was measured at a speed of 500 RPM. Figure 23(a) is a BEMF waveform before the test, and its Root Mean Square (RMS) value is 19.37 V_{rms}.

Figure 23(b) shows the BEMF waveform after the test, and its RMS value is 8.5 V_{rms}. Therefore, the BEMF decreased by 56.1% after the test as compared to its value before the test.

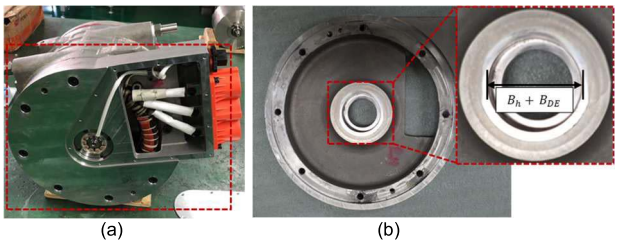

FIGURE 19. Machining for application of DEF condition, (a) base motor, (b) Machining of the bearing pocket in the rear cover.

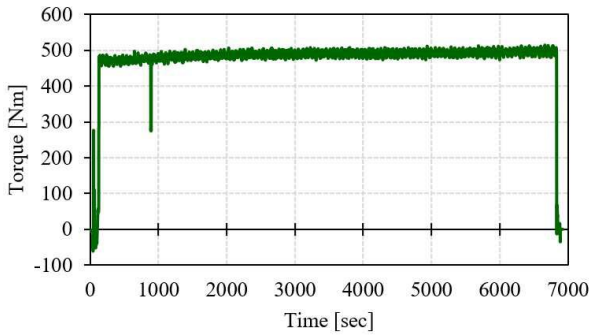

FIGURE 20. Torque (electric-axle).

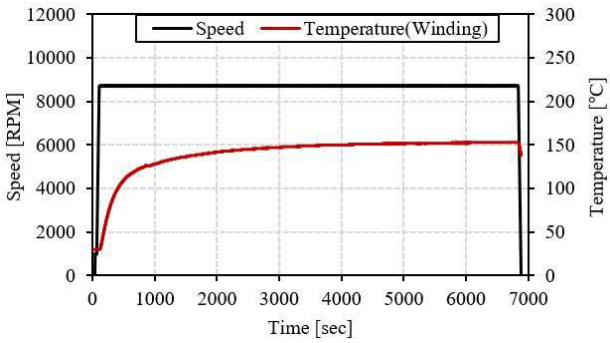

FIGURE 21. Speed and winding temperature.

C. ANALYSIS OF THE IDF OF PERMANENT MAGNETS

Since BEMF decreased after the test, the DEF motor was decomposed to analyze the cause. Figure 24(a) is the rotor before the load test, and Figure 24(b) shows the rotor after the load test. As shown in Figure 24(b), a hot spot occurred due to excessive heat in the rotor. As shown in Figure 24(b), the hot spot on the rotor occurred in a total of 8 bridge areas of the rotor because the number of poles of the motor is 8 poles, as shown in Figure 25. Because the length of the air gap is not constant in the DEF condition, the saturation of magnetic flux density occurs in the rotor bridge region. Figure 25 compared the iron loss obtained from the FEM analysis under the same conditions as the load test. The FEM analysis speed is 8,700 RPM, and the motor output is 50kW. Figure 25(a) shows the iron loss in the healthy condition, and Figure 25(b) shows the iron loss in the DEF condition. As shown in Figure 25(b), the iron loss increases at the same rotor position where the hot spot occurs. Also, iron loss increases in the teeth of the stator. As a result, since the heat generated due to the iron loss in the stator is transferred to

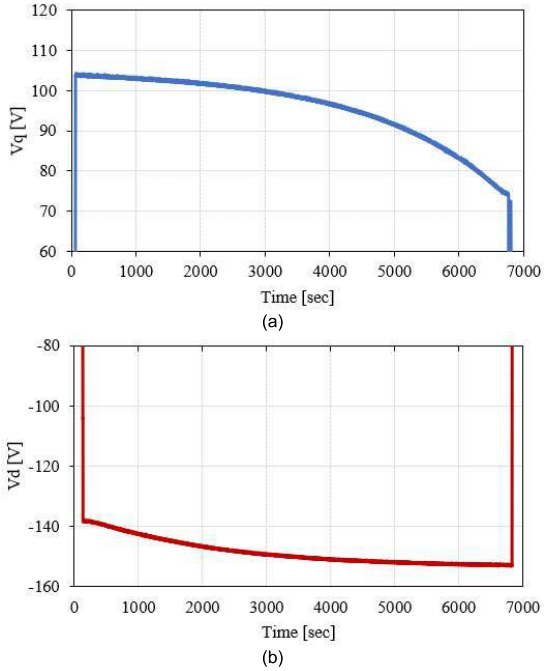

FIGURE 22. voltages of the DEF motor, (a) V_q, (b) V_d.

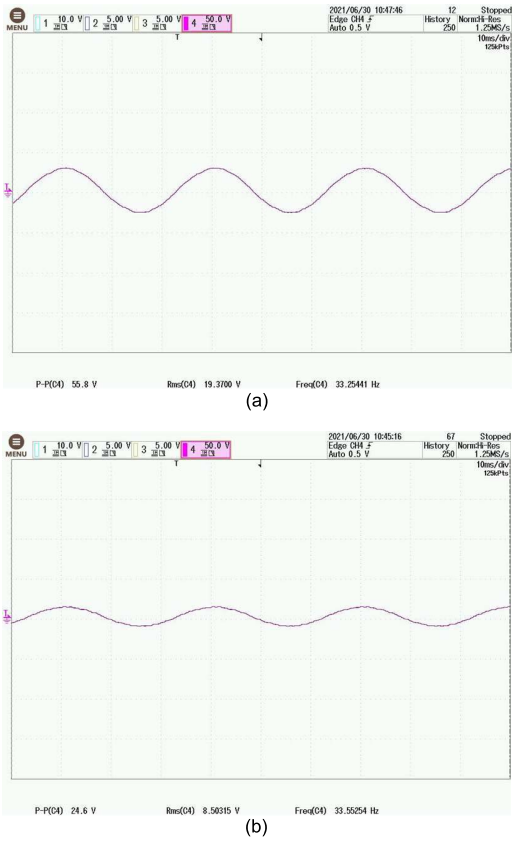

FIGURE 23. BEMF results at 500 rpm, (a) before load test, (b) after load test.

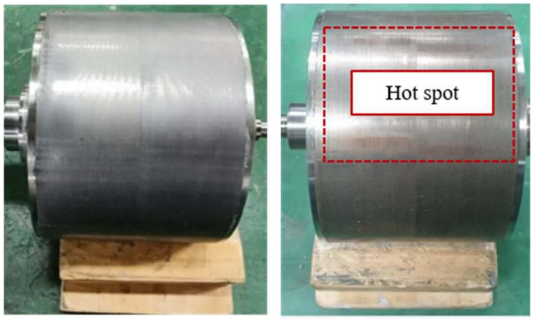

FIGURE 24. Rotor, (a) before load test, (b) after load test.

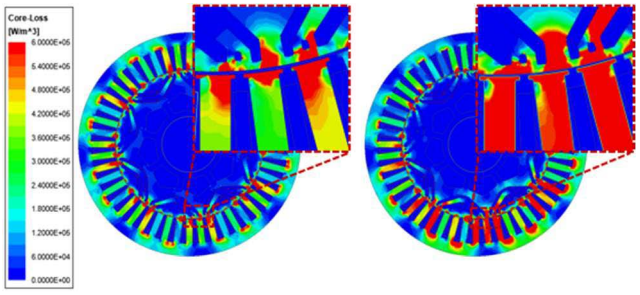

FIGURE 25. Comparison of iron loss at 8,700 RPM, (a) healthy, (b) DEF (38%).

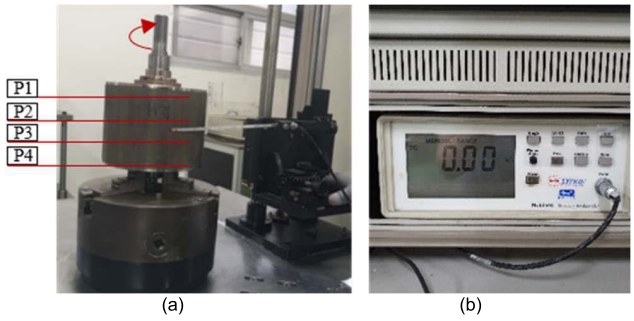

FIGURE 26. Radial flux density measurement, (a) Measurement points on the rotor, (b) gauss meter.

the rotor, the temperature of the rotor increases. As shown in Figure 26(b), the radial flux density of the rotor was measured using a gauss meter. As shown in Figure 26(a), the radial flux density was measured at P1, P2, P3, and P4 points of the rotor. Figure 27 shows the comparison between the measurement results of radial flux density before and after the load test. After the load test, since IDF occurred, the radial flux density decreased at all points P1 $\sim$ P4. In particular, in the case of Figure 27(c), the radial flux density decreased by 93.2 % after the load test as compared to the value before the load test. Since point P3 lies at the central region of the rotor along the axial direction where the heat is concentrated, the radial flux density decreased more at this point than at the other points due to DEF.

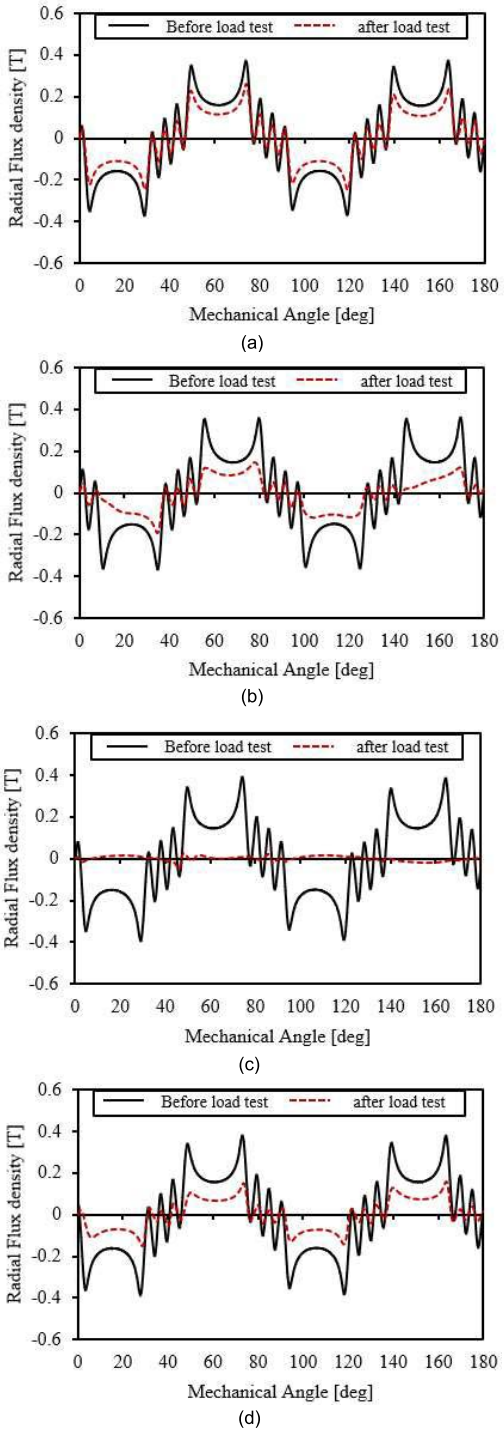

FIGURE 27. Measurement results of radial flux density, (a) P1, (b) P2, (C) P3, (d) P4.

In the case of a stator inter-turn fault, irreversible demagnetization occurs due to an instantaneous overcurrent. However, in the case of dynamic eccentricity, long-term driving of the motor in the high-speed area causes distortion of magnetic flux density, and the iron loss increases, resulting in irreversible demagnetization due to the temperature rise of the

permanent magnet. Dynamic eccentricity is implemented as shown in Figure 1(b). In addition, the test was performed while monitoring the winding temperature, V_d and V_q voltages in real-time as shown in Figure 21 and Figure 22. Test results showed that the temperature of the winding was normal. However, due to dynamic eccentricity, irreversible de-magnetization of the permanent magnet occurred.

VI. CONCLUSION

In this study, the iron loss characteristics of IPMSM for EVs traction according to the DEF condition and the irreversible demagnetization of the permanent magnets are analyzed. In the case of the DEF condition, since the length of the air gap is not constant, the waveform of the air gap flux density is unbalanced. As a result, the harmonic component due to the distortion of the magnetic flux density increases, thereby increasing the iron loss. In particular, as the iron loss increases in the DEF condition, the temperature inside the motor rises rapidly, causing irreversible demagnetization of the permanent magnets. Finally, an electric-axle load test was performed to verify the fault mechanism of the IDF by driving it for a long time in the DEF condition. As a result of the load test, BEMF decreased by 56.1% after the test due to the IDF as compared to before the test. In conclusion, DEF not only affects the noise and vibration of the electric motor but also IDF occurs due to an increase in the iron loss of the electric motor when continuously driven in DEF condition. The results of this study will be helpful to analyze the electromagnetic ch-aracteristics of IPMSM due to DEF.

REFERENCES

[1] Y.-H. Hwang and J. Lee, "HEV motor comparison of IPMSM with Nd sintered magnet and heavy rare-earth free injection magnet in the same size," *IEEE Trans. Appl. Supercond.*, vol. 28, no. 3, pp. 1–5, Apr. 2018.

[2] K. C. Kim, "A novel calculation method on the current information of vector inverter for interior permanent magnet synchronous motor for electric vehicle," *IEEE Trans. Mag.*, vol. 50, no. 2, pp. 829–832, Feb. 2014.

[3] J. Hur, "Characteristic analysis of interior permanent-magnet synchronous motor in electrohydraulic power steering systems," *IEEE Trans. Ind. Electron.*, vol. 55, no. 6, pp. 2316–2323, Jun. 2008.

[4] Y.-H. Jung, M.-R. Park, K.-O. Kim, J.-W. Chin, J.-P. Hong, and M.-S. Lim, "Design of high-speed multilayer IPMSM using ferrite PM for EV traction considering mechanical and electrical characteristics," *IEEE Trans. Ind. Appl.*, vol. 57, no. 1, pp. 327–339, Jan. 2021.

[5] H.-J. Kim and C.-S. Lee, "Shape parameters design for improving energy efficiency of IPM traction motor for EV," *IEEE Trans. Veh. Technol.*, vol. 70, no. 7, pp. 6662–6673, Jul. 2021.

[6] K.-C. Kim, "A novel magnetic flux weakening method of permanent magnet synchronous motor for electric vehicles," *IEEE Trans. Magn.*, vol. 48, no. 11, pp. 4042–4045, Nov. 2012.

[7] F. Xie, C. Qiu, and Q. Zhe, "Optimal speed–torque control of asynchronous motor for electric cars in the field-weakening region based on voltage vector optimization," *IEEE Trans. Power Electron.*, vol. 37, no. 1, pp. 830–842, Jan. 2022.

[8] M. S. Toulabi, J. Salmon, and A. M. Knight, "Concentrated winding IPM synchronous motor design for wide field weakening applications," *IEEE Trans. Ind. Appl.*, vol. 53, no. 3, pp. 1892–1900, May/Jun. 2017.

[9] Z. Ullah, S.-T. Lee, and J. Hur, "A torque angle-based fault detection and identification technique for IPMSM," *IEEE Trans. Ind. Appl.*, vol. 56, no. 1, pp. 170–182, Jan. 2020.

[10] K.-C. Kim, S.-B. Lim, D.-H. Koo, and J. Lee, "The shape design of permanent magnet for permanent magnet synchronous motor considering partial demagnetization," *IEEE Trans. Magn.*, vol. 42, no. 10, pp. 3485–3487, Oct. 2006.

[11] B.-H. Lee, J.-W. Jung, and J.-P. Hong, "An improved analysis method of irreversible demagnetization for a single-phase line-start permanent magnet motor," *IEEE Trans. Magn.*, vol. 54, no. 11, pp. 1–5, Nov. 2018.

[12] K.-T. Kim, J.-K. Park, J. Hur, and B.-W. Kim, "Comparison of the fault characteristics of IPM-type and SPM-type BLDC motors under inter-turn fault conditions using winding function theory," *IEEE Trans. Ind. Appl.*, vol. 50, no. 2, pp. 986–994, Mar. 2014.

[13] J.-K. Park, C.-L. Jeong, S.-T. Lee, and J. Hur, "Early detection technique for stator winding inter-turn fault in BLDC motor using input impedance," *IEEE Trans. Ind. Appl.*, vol. 51, no. 1, pp. 240–247, Jan. 2015.

[14] P. Zhang, K. Li, S. Yu, and D. Yu, "A novel fault diagnosis technique of interturn short-circuit fault for SRM in current chopper mode," *IEEE Trans. Ind. Electron.*, vol. 69, no. 3, pp. 3037–3046, Mar. 2022.

[15] C. Zeng, S. Huang, J. Lei, Z. Wan, and Y. Yang, "Online rotor fault diagnosis of permanent magnet synchronous motors based on stator tooth flux," *IEEE Trans. Ind. Appl.*, vol. 57, no. 3, pp. 2366–2377, May 2021.

[16] B. M. Ebrahimi, M. Javan Roshtkhari, J. Faiz, and S. V. Khatami, "Advanced eccentricity fault recognition in permanent magnet synchronous motors using stator current signature analysis," *IEEE Trans. Ind. Electron.*, vol. 61, no. 4, pp. 2041–2052, Apr. 2014.

[17] J.-K. Park and J. Hur, "Detection of inter-turn and dynamic eccentricity faults using stator current frequency pattern in IPM-type BLDC motors," *IEEE Trans. Ind. Electron.*, vol. 63, no. 3, pp. 1771–1780, Mar. 2016.

[18] B. Ebrahimi, J. Faiz, and M. J. Roshtkhari, "Static-, dynamic-, and mixed-eccentricity fault diagnoses in permanent-magnet synchronous motors," *IEEE Trans. Ind. Electron.*, vol. 56, no. 11, pp. 4727–4739, Nov. 2009.

[19] L. Ji and X. Ma, "Vibration mechanism and compensation strategy of magnetic suspension rotor system under unbalanced magnetic pull," *IEEE Access*, vol. 10, pp. 31235–31243, 2022.

[20] Y. Zhou, X. Bao, C. Di, and L. Wang, "Analysis of dynamic unbalanced magnetic pull in induction motor with dynamic eccentricity during starting period," *IEEE Trans. Magn.*, vol. 52, no. 7, pp. 1–4, Jul. 2016.

[21] C. H. Kang, K. J. Kang, J. Y. Song, Y. J. Cho, and G. H. Jang, "Axial unbalanced magnetic force in a permanent magnet motor due to a skewed magnet and rotor eccentricities," *IEEE Trans. Magn.*, vol. 53, no. 11, pp. 1–5, Nov. 2017.

[22] D. Kim, M. D. Noh, and Y. W. Park, "Unbalanced magnetic forces due to rotor eccentricity in a toroidally wound BLDC motor," *IEEE Trans. Magn.*, vol. 52, no. 7, pp. 1–4, Jul. 2016.

[23] P. Frauman, A. Burakov, and A. Arkkio, "Effects of the slot harmonics on the unbalanced magnetic pull in an induction motor with an eccentric rotor," *IEEE Trans. Magn.*, vol. 43, no. 8, pp. 3441–3444, Aug. 2007.

[24] X. Jin, M. Zhao, T. W. S. Chow, and M. Pecht, "Motor bearing fault diagnosis using trace ratio linear discriminant analysis," *IEEE Trans. Ind. Electron.*, vol. 61, no. 5, pp. 2441–2451, May 2014.

[25] R. R. Schoen, T. G. Habetler, F. Kamran, and R. G. Bartfield, "Motor bearing damage detection using stator current monitoring," *IEEE Trans. Ind. Appl.*, vol. 31, no. 6, pp. 1274–1279, Nov. 1995.

[26] M. Yang, N. Chai, Z. Liu, B. Ren, and D. Xu, "Motor speed signature analysis for local bearing fault detection with noise cancellation based on improved drive algorithm," *IEEE Trans. Ind. Electron.*, vol. 67, no. 5, pp. 4172–4182, May 2020.

[27] Y. Wang, K. Liu, W. Hua, C. Zhang, Z. Wu, and H. Zhang, "Analysis and detection of rotor eccentricity in permanent magnet synchronous machines based on linear Hall sensors," *IEEE Trans. Power Electron.*, vol. 37, no. 4, pp. 4719–4729, Apr. 2022.

[28] H. Nam, K.-H. Ha, J.-J. Lee, J.-P. Hong, and G.-H. Kang, "A study on iron loss analysis method considering the harmonics of the flux density waveform using iron loss curves tested on Epstein samples," *IEEE Trans. Magn.*, vol. 39, no. 3, pp. 1472–1475, May 2003.

[29] H. A. Khan, F. Khan, N. Ahmad, and J.-S. Ro, "Analysis and design of novel high speed permanent magnet machine considering magnet eddy current loss," *IEEE Access*, vol. 8, pp. 135675–135685, 2020.

[30] A. Cassat, C. Espanet, and N. Wavre, "BLDC motor stator and rotor iron losses and thermal behavior based on lumped schemes and 3-D FEM analysis," *IEEE Trans. Ind. Appl.*, vol. 39, no. 5, pp. 1314–1322, Sep. 2003.

[31] V. Ruuskanen, J. Nerg, M. Rilla, and J. Pyrhönen, "Iron loss analysis of the permanent-magnet synchronous machine based on finite-element analysis over the electrical vehicle drive cycle," *IEEE Trans. Ind. Electron.*, vol. 63, no. 7, pp. 4129–4136, Jul. 2016.

[32] M.-S. Lim, J.-H. Kim, and J.-P. Hong, "Experimental characterization of the slinky-laminated core and iron loss analysis of electrical machine," *IEEE Trans. Magn.*, vol. 51, no. 11, pp. 1–4, Nov. 2015.

[33] S.-W. Hwang, M.-S. Lim, and J.-P. Hong, "Hysteresis torque estimation method based on iron-loss analysis for permanent magnet synchronous motor," *IEEE Trans. Magn.*, vol. 52, no. 7, pp. 1–4, Jul. 2016.
[34] D.-W. Kim, D. H. Kang, C.-H. Kim, J.-S. Kim, Y.-J. Kim, and S.-Y. Jung, "Operation characteristic of IPMSM considering PM saturation temperature," *IEEE Trans. Appl. Supercond.*, vol. 30, no. 4, pp. 1–4, Jun. 2020.

JUN-KYU KANG (Student Member, IEEE) was born in Nonsan, South Korea, in 1991. He received the B.S. and M.S. degrees in electrical engineering from Hanbat National University, Daejeon, South Korea, in 2016 and 2019, respectively. He is currently pursuing the Ph.D. degree with the Department of Electrical Engineering, Incheon National University, Incheon, South Korea.

From 2018 to 2021, he was a Researcher at the Research and Development Center, Mcsys Company Ltd., Incheon, where he worked on the development of electric vehicle traction motor system. His research interests include motor design, motor control, and fault diagnosis of motors.

JIN HUR (Fellow, IEEE) received the Ph.D. degree in electrical engineering from Hanyang University, Seoul, South Korea, in 1999.

From 1999 to 2000, he was with the Department of Electric Engineering, Texas A&M University, College Station, TX, USA, as a Postdoctoral Research Associate. From 2000 to 2001, he was a Research Professor of electrical engineering for BK21 projects at Hanyang University. From 2002 to 2007, he was the Director of the Intelligent Mechatronics Research Center, Korea Electronics Technology Institute (KETI), Puchon, South Korea, where he worked on the development of special electric machines and systems. From 2008 to August 2015, he was an Associate Professor with the School of Electric Engineering, University of Ulsan, Ulsan, South Korea. Since August, 2015, he has been a Professor with the Department of Electrical Engineering, Incheon National University, Incheon, South Korea. He has authored or coauthored over 140 publications on electric machine design, analysis and control, and power electronics. He has one pending U.S. patent and 20 pending Korean patents. His current research interests include high-performance electrical machines, modeling, drives, new concept actuators for special purposes, and numerical analysis of electromagnetic fields.

Dr. Hur became a fellow of the IEEE Industry Application Society, in 2022. He is an Associate Editor of the IEEE TRANSACTIONS ON POWER ELECTRONICS.